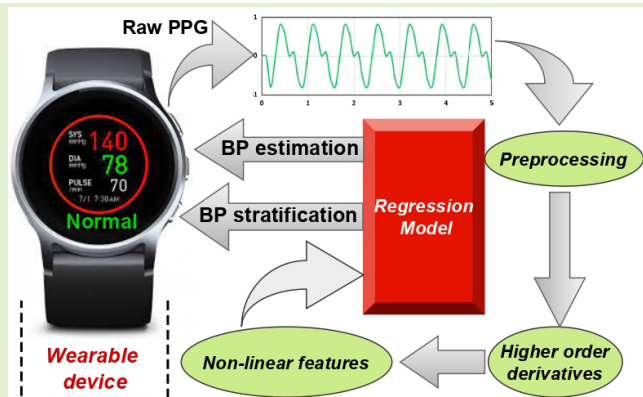


# Higher Order Derivative-Based Integrated Model for Cuff-Less Blood Pressure Estimation and Stratification Using PPG Signals

Shresth Gupta<sup>ID</sup>, Student Member, IEEE, Anurag Singh<sup>ID</sup>, Member, IEEE, Abhishek Sharma, Member, IEEE, and Rajesh Kumar Tripathy, Member, IEEE

**Abstract**—Precise blood pressure (BP) estimation is vital for diagnosing arterial hypertension and other cardiovascular ailments. The photoplethysmogram (PPG)-based cuff-less BP measurement is an alternative to the traditional cuff-based systems. The morphological, temporal, and frequency-domain-based features have been used for BP estimation in the PPG-based BP measurement systems. However, dealing with varying signal morphology and feature dependency on the fiducial points in PPG contours remains challenging and limits the performance of the existing BP estimation algorithms, especially in wearable devices. This work presents a novel approach that considers the nonlinear features of PPG signals evaluated using higher order derivatives. In particular, the PPG signal's third and fourth derivative contours are used to extract features, such as fractal dimension, bubble entropy (BE), Lyapunov exponent, and moving slope. Machine learning algorithms such as random forest (RF), extreme gradient boosting (XGBoost), and support vector regression (SVR) models are used for BP estimation using the nonlinear features of PPG signals. The estimated BP values are further categorized based on five broad classes based on the BP stratification criteria such as hypotension, normal, prehypertension, stage-I, and stage-II hypertension, respectively. The performance of the suggested approach is evaluated using PPG signals from three publicly available databases (multiparameter intelligent monitoring in intensive care (MIMIC)-I, II, and III). The proposed estimation approach has outperformed the recent existing algorithms and achieved a minimum value of mean absolute error (MAE)  $\pm$  standard deviation (STD) in (systolic BP (SBP) and diastolic BP (DBP) values) as  $0.74 \pm 2.42$  and  $0.35 \pm 1.06$ , respectively, for the MIMIC-I database. The suggested approach has also achieved grade-A on the British Hypertension Society (BHS) standard.

**Index Terms**—Blood pressure (BP) estimation, derivatives, hypertension, photoplethysmogram (PPG), sensor signal processing.



## I. INTRODUCTION

**P**HOTOPLETHYSMOGRAPHY (PPG) is an optical measurement procedure used to determine blood volume variations in the microvascular bed of target tissue [1]. The wearable technology of health monitoring, including smartwatches and wrist fitness bands, has attracted colossal

Manuscript received 20 September 2022; accepted 29 September 2022. Date of publication 10 October 2022; date of current version 14 November 2022. The associate editor coordinating the review of this article and approving it for publication was Prof. Kea-Tiong (Samuel) Tang. (*Corresponding author: Shresth Gupta.*)

Shresth Gupta, Anurag Singh, and Abhishek Sharma are with the Department of Electronics and Communication Engineering, International Institute of Information Technology (IIIT), Naya Raipur, Naya Raipur, Chhattisgarh 493661, India (e-mail: shresth@iitnr.edu.in).

Rajesh Kumar Tripathy is with the Department of Electrical and Electronics Engineering, BITS Pilani, Hyderabad, Telangana 500078, India. Digital Object Identifier 10.1109/JSEN.2022.3211993

consumer interest over the past few years. Advanced wearable devices not only focus on simple measurements of fitness tracking such as the number of steps taken per day or heart rate but also monitor some vital physiological parameters of the body such as blood pressure (BP), blood oxygen saturation level, glucose measures, stress level, and heart rate variability [2]. Estimating continuous BP and heart rate monitoring using noninvasive PPG signals has gained momentum in recent years due to wearable and sensor technology advancements. BP monitoring is essential to assess the overall health and most illnesses and disorders. It also aids in diagnosing and treating high BP (hypertension) and associated diseases such as preeclampsia and pregnancy-induced hypertension. It is always advised by the physician to monitor the BP at home if the patient has hypertension, coronary heart disease, diabetes, or renal disease [3], [4]. Various state-of-the-art methods such

as feature engineering and neural network model approaches are used to accurately obtain BP estimations and hypertension detection close to clinical standards. Pulse transit time (PTT) was the most successful calibration-free approach obtained from an electrocardiograph (ECG) and PPG to estimate BP using regression [5]. Deep learning methods are also used in this segment to use PTT and some other temporal features using long short-term memory (LSTM) [6] and artificial neural network (ANN)-LSTM [7] framework to achieve closer accuracy. A significant shortcoming of this approach is the synchronous collection of ECG and PPG signals to accurately calculate PTT and a tedious burden in signal processing for preprocessing both the signals. Hence, the solution started with a single PPG sensor-based BP estimation and is currently in the prototype stage, which needs more exploration of its potential. Liu et al. [8] extracted features from PPG's first and second derivatives to estimate BP using support vector regression (SVR). Hasanzadeh et al. [9] proposed modified normalized pulse volume (mNPV) and heart rate variability features to correlate with target BP values. Recent work includes attention mechanism with recurrent neural network (RNN) for 22 characteristic PPG features [10]. In a similar context, the same authors used first and second derivative-based features with RNN to yield better results for a single PPG-based estimation framework [11]. The use of large artery stiffness index as a feature also yielded a good result for BP estimation in a recently reported algorithm which was purely a key-point-dependent approach [12]. Some authors used PPG spectrograms and visibility graph data to exploit pretrained deep learning models for BP estimation [13], [14]. However, conversion of PPG waveform into corresponding transform images requires tedious image processing tasks for small wearable devices. The algorithms using the first and second derivatives have partially addressed the problem of accurate fiducial point detection in morphologically varying PPG signals. It helps in highlighting the appearance of fiducial points. However, this is helpful in only those PPG cycles in which at least an absolute systolic peak is visible. This work addresses the above concerns further by proposing a fiducial point-independent BP estimation algorithm for improved results. This work uses PPG's holistic nonlinear dynamics and moving slope features by exploiting its third and fourth derivatives for BP estimation. The proposed features are well-derived from the whole PPG segment instead of specific points in contour, which addresses the problem of fiducial points' detection. Popular machine learning techniques are optimized, and their suitable variant is used in obedience with the derived features to deliver improved results for BP estimation of the proposed method is done extensively using publicly available databases to demonstrate the robustness and reliability of the proposed work.

## II. MOTIVATION

The natural morphology of PPG contains different fiducial points, which indicates a different circulatory event of BP. A significant challenge in PPG signal processing is its varying morphology due to different artifacts when the PPG signals are recorded during various physical activities [15]. Some morphologically distorted PPG signals are shown in Fig. 1, which

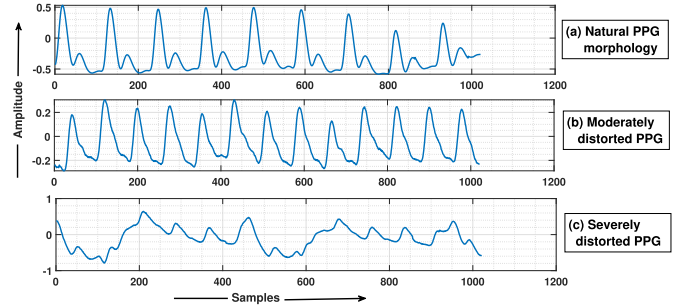


**Fig. 1.** Varying PPG morphology. (a) PPG cycles in their natural morphology. (b) Moderately affected PPG cycles with high-frequency noise. (c) Severely distorted PPG cycles due to motion artifacts and other noise.

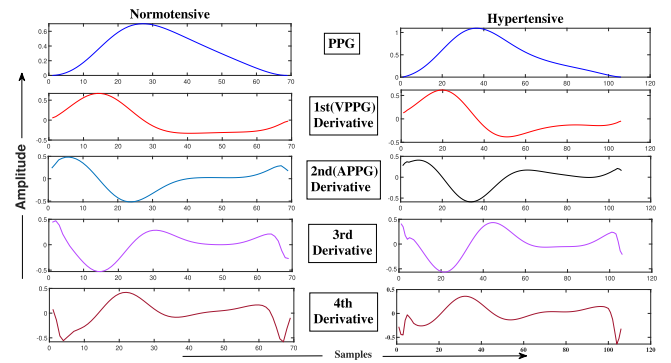


**Fig. 2.** Variation in single PPG cycle and its derivatives for normotensive (left) and hypertensive subject (right).

are sometimes classified as appropriate and inappropriate PPG [16]. Most of the works mentioned above [8], [9], [10], [11] rely on accurately detecting the physiological fiducial points to derive feature sets from every PPG cycle. However, it is practically challenging to obtain these fiducial points accurately for the artifact-contaminated PPG signals [see Fig. 1(b) and (c)]. Furthermore, the performance of a BP estimation algorithm may be reduced due to the presence of artifacts in the PPG data. Motivated by the shortcomings of the methods mentioned above, we have proposed a fiducial-point-independent BP estimation framework in this work.

After experimental investigation, we observed that PPG contours are similar for most subjects under different BP ranges. It is impossible to differentiate the PPG cycles in different classes using the existing features in their natural form. Even in lower order derivatives (first and second), class discrimination is not clear, as shown in Fig. 2, where the time series PPG and its first and second derivatives are shown for two BP classes, normotensive and hypertensive. Hence, we propose using higher order PPG signal (third and fourth derivatives) derivatives to extract the nonlinear features and slope variations to classify and estimate BP uniquely. In Fig. 2, it is evident that the standard PPG contour is quite similar in the time domain as well as in the first and second PPG derivatives, also called the velocity PPG (VPPG) and acceleration PPG (APPG). On the other hand, the third and fourth derivatives show visible differences between the two waveform shapes, which can be exploited in extracting significant discriminating features. Using higher order derivatives

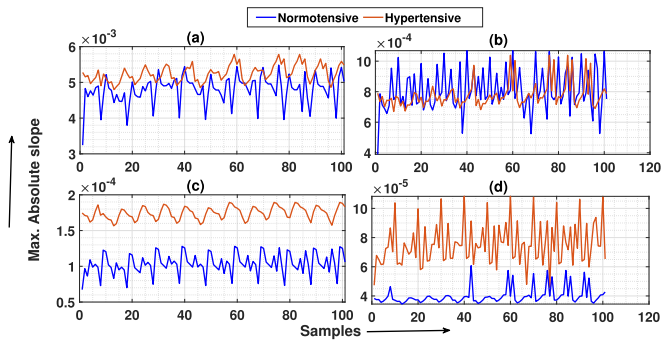


**Fig. 3.** Plot of moving slope values of PPG cycles calculated using three-point sliding window for normotensive and hypertensive PPG episodes under 100 samples from the first to fourth derivatives for analyzing the discriminating behavior of the two classes. **(a)** VPPG (first derivative). **(b)** APPG (second derivative). **(c)** Third derivative. **(d)** Fourth derivative.

of PPG helps capture all its slope changes from its VPPG and APPG versions. For signals with the same form and amplitude, it is discovered that the amplitude of the  $n$ th derivative of a peak is inversely proportional to the  $n$ th power of its width. As a result, differentiation effectively discriminates against more prominent peaks, and discrimination increases with increasing order of differentiation [17]. This behavior is helpful for quantitative analytical applications for discrimination between two slowly varying physiological signals like PPG. To show the quantitative differences in the varying morphology of hypertensive and normotensive PPG for higher derivatives, we have calculated the moving slope values and plotted for the first derivative to the fourth derivative in Fig. 3. As can be seen in the first and second derivatives, in many instances, the absolute slope values are very close to each other in both the classes, which reveals the reasonable similarity between the contours of the two classes. On the other hand, PPG's third and fourth derivatives show significant changes in the slope values of both the classes, which highlights adequate morphological difference. In this way, we are exploiting the discriminating morphology of the PPG for the two classes in higher derivatives and promoting its nonlinear dynamics.

However, discriminating characteristics of PPG derivatives diminishes as we go further to higher derivatives, as explained in detail in Section IV-C. Hence, we restricted our analysis up to the fourth derivative in this work.

### III. METHODOLOGY

The overall framework of the proposed work is illustrated in Fig. 4. The novelty of the work lies in proposing a higher order derivative-based integrated model for BP estimation and then stratification of the estimated BP values using optimized machine learning approaches. The estimation task is obtained using a novel set of higher order PPG-derivative-based nonlinear features followed by a stratification block containing the labels for a given range of BP values as shown in Fig. 4.

#### A. Database

The performance evaluation of the proposed BP estimation framework is carried out with two widely used publicly

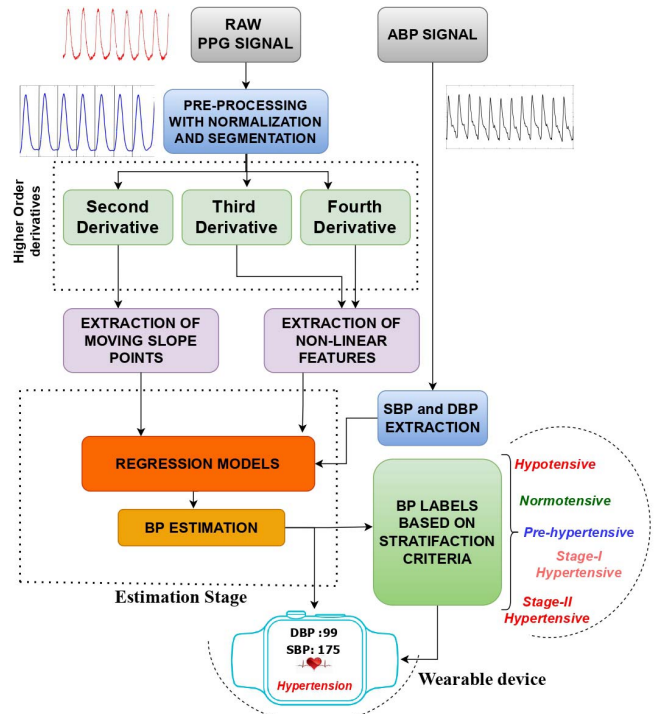


**Fig. 4.** Integrated BP estimation and stratification framework using raw PPG.

available databases: multiparameter intelligent monitoring in intensive care (MIMIC)-I, II, and III [18], [19], [20]. Most of the existing BP estimation works have used these databases as they contain various physiological signals with reference to gold standard invasive arterial BP (ABP). The MIMIC-II database contains 12 000 records, each containing synchronized measurement of ECG, PPG, and invasive ABP signal (reference BP), all sampled at 125 Hz. A subset of MIMIC-II is also available at the University of California Irvine (UCI) Machine Learning Repository [19] and has also been used in BP estimation works. Another database MIMIC-I is hosted at Physionet and has records of 39 patients with simultaneous ECG, PPG, and ABP signals blue sampled at 500 Hz [18]. MIMIC-I is also used at the same sampling frequency as MIMIC-II, i.e., 125 Hz, to maintain uniformity throughout the databases. However, to achieve 125-Hz sampling frequency, the MIMIC-I database was downsampled from the original recording at 500 Hz with 12-bit precision. Although there are 93 patient records available in MIMIC-I, the records with simultaneous measurements of the three signals are taken. Similarly, MIMIC-III is a rich database containing records of more than 40 000 patients, among which 510 patient's data are taken after discarding anomalies. Systolic BP (SBP) and diastolic BP (DBP) signals are extracted using the ABP signal. After careful investigation, datasets with duplicate records, saturated amplitudes, and discontinuities were discarded.

#### B. Preprocessing

To eliminate baseline wandering and other associated noise from raw PPG, we used the tunable  $Q$ -factor wavelet transform (TQWT) denoising scheme [7], [21]. Apart from taking

advantage of the wavelet-based denoising, this approach exploits the PPG signal's oscillatory and transient behavior with its customizable tuning, redundancy, and decomposition parameters. Furthermore, in comparison to other approaches, preprocessing the critical signals with TQWT offers several benefits, including improved phase response, increased computational efficiency, adaptivity in various signal-to-noise ratio regimes, and even handling the nonstationary artifacts [7]. Since the second database [19] is a subset of the MIMIC-II database, it is already preprocessed and ready to analyze PPG episodes with simultaneous ECG and ABP signals. Thus, preprocessing is done for the MIMIC-I and III databases only to remove the associated artifacts. In preprocessing, by changing the  $Q$  value, the wavelet decomposition sub-bands can be shifted in the frequency domain, which can be used to effectively remove the baseline wandering artifact while preserving the morphological contour shape as much as possible. For a raw PPG episode denoted as  $r(t)$ , the TQWT is performed with ten-level decomposition using the equation

$$W^j = \text{TQWT}(r(t), Q, r, J). \quad (1)$$

Here, the length of  $r(t)$  should be even,  $Q \geq 1$ ,  $r > 1$ ,  $J = 10$ , where  $Q$  is a tuning factor given by the ratio of center frequency to the bandwidth of given PPG.  $r$  is the redundancy factor which means total oversampling rate of the transform. The output  $W^j$  represents the low- and high-pass wavelet coefficients produced by level  $j$  filter bank. The maximum quality factor  $Q$  is selected from a look table which contains maximum 3-dB frequency and center frequency for a given peak frequency of PPG signal. A default redundancy factor  $r = 3$  is used. After removing residues of coefficients related to high-frequency noise and applying soft rigrsure thresholding, we reconstruct our clean PPG signal using the inverse TQWT

$$y = \text{TQWT}^{-1}(W^j, Q, r, J) \quad (2)$$

where  $W^j$  is the remaining wavelet coefficients after removing high-frequency residues.

### C. Extraction of Nonlinear Features Using Higher Order Derivatives

Fig. 2 shows a dynamic variation in PPG contour in its third and fourth derivatives. Equations (1)–(4) are used to calculate the derivatives of PPG up to the fourth level, where  $p(t)$  represents a clean PPG signal that has been filtered using the TQWT approach. VPPG and APPG, which represent the blood's velocity and acceleration, respectively, were formed by the first derivation of PPG and the second. The acceleration rate or variations in acceleration over time make up the third derivative (D3) also called as "Jerk," and the rate of change of D3 is finally obtained from the fourth derivative (D4) called as "Snap" [22]. For any PPG signal, its zero-crossing before a derivative peak represents the negative peak of its original PPG, whereas zero-crossing after a derivative peak represents the positive peak of its original PPG. The mathematical interpretation of each of the derivative is given as follows (3)–(6), as shown at the bottom of the next page.

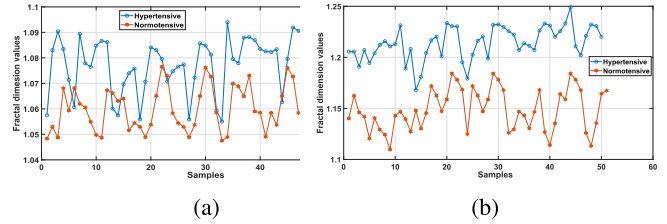


**Fig. 5.** HFD feature values for 50 segments of PPG. (a) In the third derivative of PPG. (b) In the fourth derivative of PPG.

We derived four state-of-the-art nonlinear features that can help distinguish between different classes of BP types and their values to be used as feature sets to target SBP and DBP for estimation. It is important to note that these nonlinear features do not require any key point detection in the given PPG cycle, and the computed features span one complete cycle having an accurate onset and endpoints. We used the automatic multiscale-based peak detection (AMPD) algorithm [23] for segmenting different PPG cycles. The following nonlinear features are extracted from the third and fourth derivative PPG contours.

**1) Fractal Dimension:** The fractal dimension measures a waveform's self-similarity or space-filling property, which depicts its structural complexity. Several algorithms are available to calculate the fractal dimension of a given time series pattern from which we used Higuchi's algorithm for this application due to its efficient computation for smaller segments and the number of sample points [32]. Suppose a single PPG episode of a subject represented as  $P$  is segmented into  $N$  segments and each consisting a complete cycle is denoted as  $p(0), p(1), p(2), \dots, p(N)$ . Then, time series  $p_k^m$  can be expressed as

$$\begin{aligned} p_k^m : & p(m), p(m+k), p(m+2k) \\ & \dots p(m + \text{int}[(N-k)/k])k \end{aligned} \quad (7)$$

where  $m = 1, 2, \dots, k$  is the initial time, and  $= 1, \dots, k_{\max}$  is the time interval.

The length of the curve  $L_{m(k)}$  for each  $p_k^m$  time series is calculated as (8), shown at the bottom of the next page.

$N$  is the original time series, and  $(N - 1/\text{int}[(N-m)/k].k)$  is normalization factor. The procedure in (2) is repeated for all  $k$  values, and the lengths are averaged as

$$L(k) = \frac{1}{k} \sum_{m=1}^k L(m, k). \quad (9)$$

If  $L(k)$  is plotted against  $1/k$  on a logarithmic scale, for  $k = 1, \dots, k_{\max}$ , then the data points fall on a straight line with a slope equal to the Higuchi fractal dimension (HFD) of given time series PPG given by  $(\ln(L(k))/\ln(1/k))$ . The calculated HFD from the third and fourth derivatives of PPG contours for normotensive and hypertensive patients is shown in Fig. 5(a) and (b), respectively. A clear distinction between HFD values for both BP classes can be observed in the above plots.

The obtained  $D$  values are calculated with optimum  $K_{\max} = 5$ . Factor  $D$  is a statistical coefficient representing the spatial distribution of events, and its value close to 1 shows more

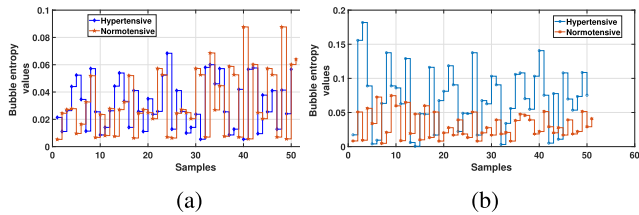


**Fig. 6.** BE feature values for 50 segments of PPG. (a) In the third derivative of PPG. (b) In the fourth derivative of PPG (calculated with embedding dimension  $m = 5$  in both the cases).

self-similarity and linear distribution. Here, higher values of  $D$  for hypertensive contour show its higher complexity than normal subjects. The fourth derivative is more prominent to show the difference in values for the two classes and can correlate well with SBP and DBP.

**2) Bubble Entropy:** Bubble entropy (BE) is a recent state-of-the-art entropy measure that is almost free of parameters. This entropy measure is based on the concept of permutation entropy which uses the ranking of vectors in embedding space. The algorithm uses a bubble sort scheme for ordering and counting the vectors in embedding space [33]. Unlike other entropy schemes, BE ensures better stability and good discriminating power for most physiological signals. The BE is calculated using the expression

$$\text{BE}_n = (H_{\text{swaps}}^{m+1} - H_{\text{swaps}}^m)/\log(m+1)/(m-1). \quad (10)$$

Here, the normalization factor is given by the difference in the maximum entropy which is  $\log[1 + m(m-1)/2]$  and  $\log[1 + m(m+1)/2]$  for embedding dimension  $m+1$ . There is no need to feed the scaling factor, which is eliminated in this measure while the embedding dimension  $m = 5$  is used for this application, since the sample entropy along with BE exhibits higher discriminating power in the range  $m = 2-6$ . The obtained entropy of 50 segments is shown in Fig. 7. Like HFD, the BE discriminates between the two BP classes with a higher value for hypertensive contours. The fourth derivative statistics pattern in Fig. 6(b) provides a clear picture of enhanced randomness in waveform and entropy for hypertensive subjects. The randomness can collectively

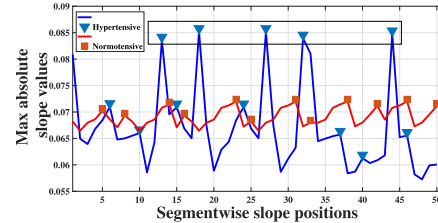


**Fig. 7.** Maximum absolute slope values for PPG segments of normotensive and hypertensive subject (the peaks of hypertensive slopes highlighted within rectangle).

correlate with the mean arterial pressure for the whole segment, improving the estimation.

**3) Lyapunov Exponent:** Like other physiological signals such as ECG and electroencephalogram (EEG), the pulse wave or PPG also exhibits the property of chaos, as seen in its higher derivative morphology. To capture the chaotic behavior of a time series signal, the Lyapunov exponents are a better measure that provides the separation rate of infinitesimally close trajectories [34] given by the expression

$$\delta x(t) \approx e^{\lambda t} |\delta x_0| \quad (11)$$

where  $\lambda$  is referred to as the Lyapunov exponent. For every segment of our PPG, the absolute value of the maximum Lyapunov exponent is calculated for the sampling frequency value as  $f_s = 125$  Hz.

**4) Moving Slope Points:** The second derivative of PPG or APPG contains multiple small waves, and the detected maxima and minima for each wave lead to five major fiducial points such as  $a-e$ , which contain the diagnostic information [22], [31]. These points and their ratio are a good index for altered arterial distensibility and stiffness. Hence, tracing the slope of the contour between these points helps identify the pulse wave pressure, which directly relates to the arterial pressure or BP. Thus, extracting moving slope points of the contour extracts all the variations of small waves of APPG. Under a three-point sliding window, we extracted all the slope points of the contour in each segment, and then the maximum absolute slope point was used as a feature. For each PPG contour denoted as segments  $c(0), c(1), c(2), \dots, c(N)$ , we calculate

$$\text{VPPG} = \frac{d(\text{PPG})}{dt} = \frac{d[p(t) - p(t-1)]}{dt} \quad (3)$$

$$\text{APPG} = \frac{d(\text{VPPG})}{dt} = \frac{d[p(t) - 2p(t-1) + p(t-2)]}{dt} \quad (4)$$

$$D3 = \frac{d(\text{APPG})}{dt} = \frac{d[p(t) - 3p(t-1) + 3p(t-2) - p(t-3)]}{dt} \quad (5)$$

$$D4 = \frac{d(D3)}{dt} = \frac{d[p(t) - 4p(t-1) + 6p(t-2) - 4p(t-3) + p(t-4)]}{dt} \quad (6)$$

$$L(m, k) = \left\{ \left( \sum_{i=1}^{\text{int}(\frac{N-m}{k})} |p[m+ik] - p[m+(i-1).k]| \right) \frac{N-1}{\text{int}(\frac{N-m}{k}).k} \right\}. \quad (8)$$

this feature as

$$MS = |\max(\text{moving slope}(c(N)))|. \quad (12)$$

**Fig. 7** demonstrates the maximum absolute slope points for both the categories of subjects. Due to the steeper contour of the hypertensive subjects, their maximum slope point is higher than the normotensive class shown within the rectangle. Thus, a clear separation of these slope points gives a meaningful discriminating feature to classify different BP classes and the calculated maximum value maps with SBP with a linear proportion.

#### D. BP Estimation Using Regression Models

After feature extraction, we normalized and applied the feature set in different regression models. Three optimized regression models, namely, random forest (RF), extreme gradient boosting (XGBoost), and SVR, are used for accurate BP estimation tasks. We have used these regression models to exploit their individual forte given below.

- 1) RF regression is used in our estimation block to deal with our nonlinear feature values. Since nonlinear parameters do not affect the performance of an RF, unlike the curve-based algorithms, if there is high nonlinearity between independent variables, RF may outperform other curve-based algorithms. Moreover, its stability and less impact from noise are an additional advantage to achieving accurate estimation in the proposed work [37].
- 2) Using XGBoost regressor in our proposed estimation framework adds the benefit of regularization capability, preventing the model from overfitting. Furthermore, its parallel processing capability is helpful for our work in the environment of edge computing [38].
- 3) We have used multiple PPG signal databases to test the robustness of our framework and the core idea of using a support vector regressor is to exploit its generalization capability for extensive data, robustness towards outliers, and easy implementation [39].

After obtaining continuous estimated BP values from each regression model, they are given to the stratification block containing five broad BP stratification criteria [40]. After the extraction of reference BP values from the ABP signal, the obtained SBP ranges from 84.79 to 181.7 mmHg, while the DBP covers the span of 51.48–101.25 mmHg. As per the seventh report of the Joint National Committee on Prevention, Detection, Evaluation, and Treatment of High Blood Pressure (JNC7), BP can be categorized into four major classes: normotension, prehypertension, stage-1 hypertension, and stage-2 hypertension [40]. As per the available range of lower BP values, we have added one more class in this work as hypotension. BP values below 90/60 are considered hypotensive, showing insufficient pumping pressure for the perfusion of major organs by oxygenated blood. **Table I** provides the detailed stratification criteria.

The obtained nonlinear feature set is used as a training data in the regression block. The simultaneously measured reference BP values (SBP and DBP) from the ABP signal are used in the regression section as ground truth, and using the

**TABLE I**  
BP STRATIFICATION CRITERIA

| BP Class  | BP Type              | SBP(in mmHg) | Operator | DBP(in mmHg) |
|-----------|----------------------|--------------|----------|--------------|
| Class-I   | Hypotension          | < 90         | and      | < 60         |
| Class-II  | Normotension         | 90 – 119     | or       | 60 – 79      |
| Class-III | Prehypertension      | 120 – 139    | or       | 80 – 89      |
| Class-IV  | Stage-1 hypertension | 140 – 159    | or       | 90 – 99      |
| Class-V   | Stage-2 hypertension | ≥ 160        | or       | ≥ 100        |

**TABLE II**  
ESTIMATION RESULTS OBTAINED USING DIFFERENT REGRESSION MODELS (IN MAE ± STD)

| Database  | BP type | Random forest | XGboost     | SVR          |
|-----------|---------|---------------|-------------|--------------|
| MIMIC-I   | SBP     | 0.74 ± 2.42   | 2.54 ± 3.93 | 6.80 ± 15.99 |
|           | DBP     | 0.35 ± 1.06   | 1.17 ± 1.77 | 4.31 ± 6.51  |
| MIMIC-II  | SBP     | 1.69 ± 3.76   | 3.07 ± 4.95 | 4.92 ± 14.04 |
|           | DBP     | 0.77 ± 1.81   | 1.36 ± 2.21 | 2.44 ± 10.64 |
| MIMIC-III | SBP     | 1.30 ± 4.05   | 2.2 ± 4.95  | 3.46 ± 6.21  |
|           | DBP     | 0.56 ± 1.70   | 1.46 ± 2.60 | 2.81 ± 3.56  |

stratification criteria given in **Table I**, the values are converted into the numeric labels between 1 and 5 for five different classes which may be given to the wearable device to display that BP class.

#### IV. EXPERIMENTAL RESULTS

The performance evaluation of the proposed method was done using the MIMIC-I and II databases. Novel features from higher order PPG derivatives were extracted and fed to the advanced ML algorithms for estimating BP values. RF is used with 100 estimators (number of trees in the ensemble), SVR with the Gaussian radial basis function, while XGboost is used with 1000 estimators, maximum depth = 7, and learning rate = 0.1. After feature extraction, a total sample size of input data extracted from the MIMIC-I, II, and III databases contains 21 290 742, 4 594 474, and 19 753 777 samples, respectively. The estimation performance of three popular regression models with both the database is provided in **Table II** with the evaluation metric as mean absolute error (MAE), standard deviation (STD), and coefficient of determination ( $r^2$ ).

The MAE is computed by comparing the estimated BP values with the ground-truth values after fitting the training data with the target BP values. The residuals' STD determines how widely the data points straddle the regression line, and the outcome is used to calculate the predictability error of the regression line.  $r^2$ , which ranges from 0 to 1, expresses how accurately a statistical model forecasts a result.  $r^2$  can be seen as the percentage of variation in the dependent variable that the statistical model predicts [41]. After analyzing with these parameters, the best estimation is obtained using RF regressor with MAE ± STD of 1.69 ± 3.76 and 0.77 ± 1.81 for SBP and DBP, respectively, in the MIMIC-II database, while for estimation with the MIMIC-I database a more accurate result of 0.74 ± 2.42 and 0.35 ± 1.06 for SBP and DBP, respectively, followed by 1.30 ± 4.05 and 0.56 ± 1.706 with the MIMIC-III database. The best results are obtained with RF

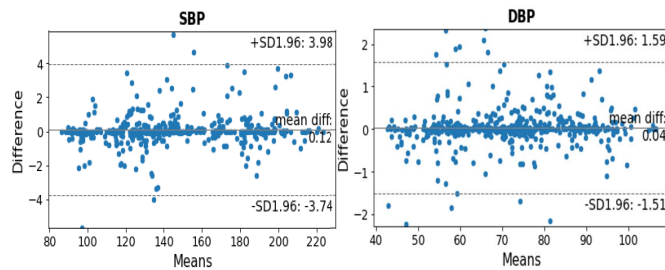


**Fig. 8.** Bland-Altman plot of difference between predicted and true values for SBP and DBP (for 1000 data predictions) with obtained mean difference of 0.12 and 0.04, respectively.

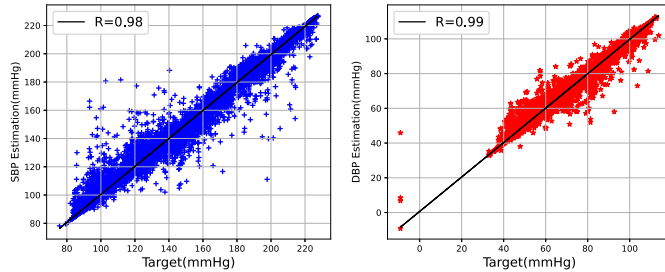


**Fig. 9.** Scatter plot of SBP and DBP after regression with RF analyzed for the MIMIC-II database (best fit line (SBP)  $Y = 1.40 + 98X$  and (DBP)  $Y = 0.63 + 0.99X$ ).

regressor compared with XGboost and SVR since XGboost and SVR are more sensitive toward the outliers and cannot handle the heavy outliers of abnormal BP values. Fig. 8 shows the Bland—Altman plot of 1000 error points (predicted value—true value) after regression with our best model. Out of 1000 error points, only few error points in DBP and SBP deviate above the agreement line under 95% confidence interval with little mean differences of 0.12 for SBP and 0.04 for DBP. Moreover, the arrangement of the sequential trees in XGboost and complex kernel for SVR makes the training time longer than RF. In addition, RF can reduce the high variance from a flexible model using a combined form of many trees in one ensemble model [37].

The scatter plot after regression with RF is shown in Fig 9. As can be seen in the plot of SBP estimation, it contains more outliers than DBP due to the high variance in SBP data. A higher  $r^2$ , i.e., 0.98 for SBP and 0.99 for DBP, indicates all the features' substantial contribution toward mapping with ground target values. The frequency of errors can be seen in Fig. 10. Here, the motive of taking error frequency is to locate the count of similar errors after prediction. As can be seen, most of the error counts are saturated near zero, which demonstrates the low MAEs obtained during estimation.

#### A. Significance of the Proposed Higher Order Features

To demonstrate the significance of the proposed higher derivative-based nonlinear features regarding BP estimation, we performed a performance comparison analysis with the existing popular temporal features. A list of state-of-the-art temporal features extracted for comparison using PPG and its first and second derivatives are listed in Table III. The

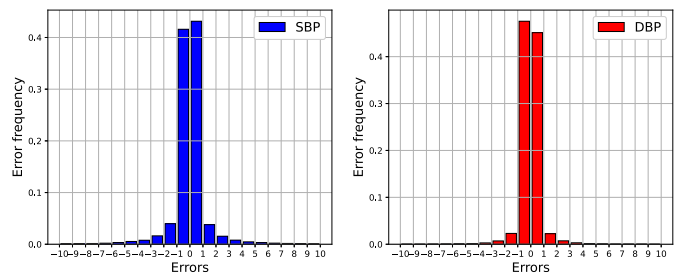


**Fig. 10.** Frequency of error after regression with RF for SBP and DBP (MIMIC-II database).

**TABLE III**  
STATE-OF-THE-ART TEMPORAL FEATURES FROM PPG AND ITS FIRST AND SECOND DERIVATIVES EXTRACTED FOR COMPARISON

| Feature              | Description   |
|----------------------|---|
| Crest time           | Systolic peak distance from origin [25]                               |
| Crest time (VPPG)    | Distance between origin to peak of VPPG [25]                          |
| $D_{dicrotic}$       | Distance of dicrotic notch from origin [26]                           |
| LASI                 | Inverse of the distance between systolic peak and dicrotic notch [27] |
| $A_s$                | Amplitude of systolic peak [28]                                       |
| $A_{dic}$            | Amplitude of dicrotic notch [28]                                      |
| Reflection Index(RI) | $A_s/A_{dic}$ [28]  |
| $A_b/A_a$            | Amplitude ratio of point b and a from APPG [30]                       |
| $A_e/A_a$            | Amplitude ratio of point e and a from APPG [23]                       |
| Wavefrom area        | Area under the curve of systole and diastole region [26]              |

necessary key points are detected for every segmented cycle to derive various temporal features. The first and second derivatives of the cycle are used to highlight the appearance of fiducial points. For key point detection, we followed the approach suggested in [9].

To bring out the significance of the proposed features in a statistical manner, we computed the regressor's feature importance of both the existing temporal features and the proposed nonlinear features with sorting by permutation importance. Permutation importance represents the decrements in model score after randomly shuffling the feature value by 1. The permutation importance approach does not require retraining of the model after permuting each column; we only need to rerun the perturbed test samples through our already trained model [44]. Fig. 11 shows the ranking of each feature after regression with the best performing model in this work, i.e., RF. The data used in regression and classification contain both appropriate and inappropriate PPG signals. The term appropriate PPG is used for PPG cycles having all the available fiducial points to extract the features. As discussed in Section III-B, most of the distortions present in PPG signals are rectified by our preprocessing algorithm. For severely distorted PPG signals in which the key points are not observable, the temporal features (depicted in Table III) yield inconsistent values due to the absence of diastolic peaks.

It can be observed from the amplitude of importance that the fractal dimensions of the third and fourth derivatives represented as FD1 and FD2, respectively, are found to be highly significant and discriminative. As shown in Fig. 5, the

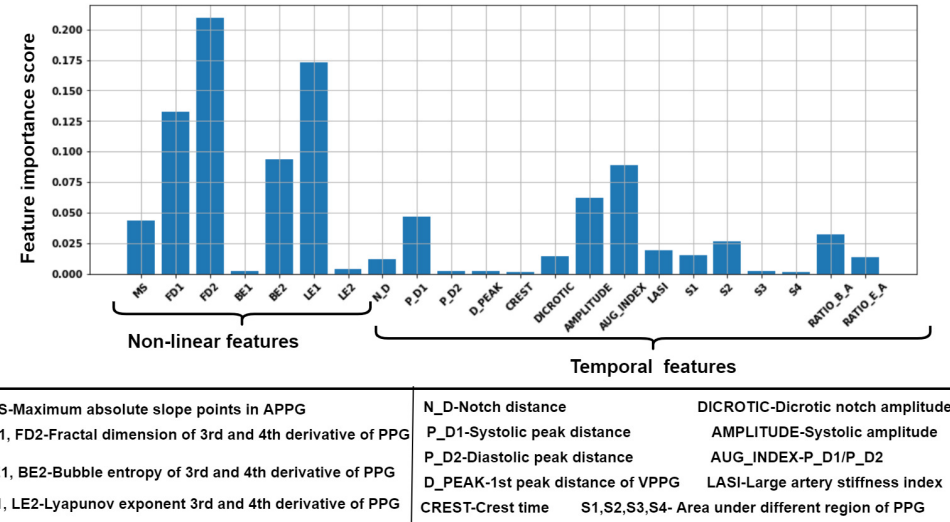


**Fig. 11.** Feature importance computed under permutation sorting for temporal and proposed nonlinear features after performing regression using RF (MIMIC-II database).

obtained ranges of fractal values are in different ranges for the normotensive and hypertensive cases separating each other and it is more prominent when calculated for the fourth derivative. Furthermore, BE (BE2), calculated from the fourth derivative, and moving slope feature MS also demonstrate remarkable feature importance compared with the temporal features.

## *B. Comparison With Existing Methods*

This section presents a comparative analysis between the proposed framework and similar existing techniques. We compared our quantitative results with other reported results under the same database segment as shown in [Table IV](#). The comparison is made in terms of estimation error ( $MAE \pm STD$ ) and Pearson correlation coefficient ( $r$ ) for both SBP and DBP. It can be observed that when compared with the existing works, we obtained the highest  $r = 0.98$  and  $r = 0.99$  for SBP and DBP, respectively, in the case of the MIMIC-II database. In terms of  $MAE \pm STD$  too, the proposed method achieves the least estimation error of  $0.74 \pm 2.42$  and  $0.35 \pm 1.06$  for SBP and DBP, respectively, using the MIMIC-I database compared with other methods in [Table IV](#). For quantitative comparison with earlier proposed features, we extracted all the features provided in [Table IV](#) using PPG signal from the benchmark dataset, i.e., MIMIC-II, and also extracted the proposed nonlinear features. After estimation with the best performing regressor (RF), we achieved an  $MAE \pm STD$  of  $1.69 \pm 3.76$  for SBP and  $0.77 \pm 1.81$  for DBP which is far better compared with the  $MAE \pm STD$  of  $8.22 \pm 10.38$  and  $4.17 \pm 4.22$  for SBP and DBP, respectively, by estimation using linear temporal features. So, overall, the proposed technique fairs significantly better than the existing approaches in BP estimation. In addition, when compared with the existing BP estimation approaches, which use other physiological signals also along with PPG [5], [6], [7], the proposed approach uses only a single PPG signal which eliminates the requirement for simultaneous measurement of PPG and ECG or any other physiological signals for estimation with adequate

**TABLE IV**  
**BP ESTIMATION PERFORMANCE COMPARISON  
 WITH OTHER APPROACHES**

| Methods         | Database  | SBP  |       |       | DBP  |      |       |
|-----------------|-----------|------|-------|-------|------|------|-------|
|                 |           | MAE  | STD   | $r^2$ | MAE  | STD  | $r^2$ |
| Deriv. [8]      | MIMIC-II  | 8.54 | 10.9  | —     | 4.34 | 5.8  | —     |
| PTT [5]         | MIMIC-II  | 8.21 | 5.45  | 0.48  | 4.32 | 5.52 | 0.59  |
| ANN [7]         | MIMIC-I   | 1.10 | —     | 0.99  | 0.58 | —    | 0.99  |
| Morpho. [9]     | MIMIC-II  | 8.22 | 10.38 | 0.72  | 4.17 | 4.22 | 0.78  |
| RNN [11]        | MIMIC-II  | 4.51 | 7.81  | —     | 2.6  | 4.1  | —     |
| Bi-GRU [10]     | MIMIC-II  | 2.58 | 3.35  | —     | 1.26 | 1.63 | —     |
| Specto. [14]    | MIMIC-II  | 5.95 | —     | —     | 3.41 | —    | —     |
| Visib. [13]     | MIMIC-II  | 6.17 | 8.46  | —     | 3.66 | 5.36 | —     |
| DLASI [12]      | MIMIC-I   | 2.41 | 5.26  | 0.82  | 0.41 | 1.50 | 0.99  |
| <b>Proposed</b> | MIMIC-III | 1.30 | 4.05  | 0.97  | 0.56 | 1.70 | 0.98  |
| <b>Proposed</b> | MIMIC-II  | 1.69 | 3.76  | 0.98  | 0.77 | 1.81 | 0.99  |
| <b>Proposed</b> | MIMIC-I   | 0.74 | 2.42  | 0.98  | 0.35 | 1.06 | 0.99  |

accuracy. Hence, it is helpful to enable power-efficient and computationally simple health monitoring. Moreover, the compared works [8], [9], [10], [11] use key-point-dependent features that might experience problems detecting fiducial points during morphological deviations under distorted PPG, which is not the case in our approach. Since most of the distorted PPG signals get corrected by our TQWT-based preprocessing module and the extracted higher derivative-based features are not dependent on fiducial points' detection, the proposed framework is applicable and responsive toward dynamic BP monitoring both during rest and activity conditions. The recent deep-learning-based methods [13], [14] follow the key-point-independent strategy by converting the 1-D time series PPG into its corresponding transform images for estimation. However, the reported estimation error (5.95) is higher than the proposed method (1.69). Also, these spectrogram-based methods might face an impede while converting 1-D PPG into images that can introduce estimation delay and power demand. So, it can be concluded that the proposed approach is simple, using only PPG signals and delivering better estimation and classification results. This shows the potential of all the new nonlinear features proposed for close mapping with target output.

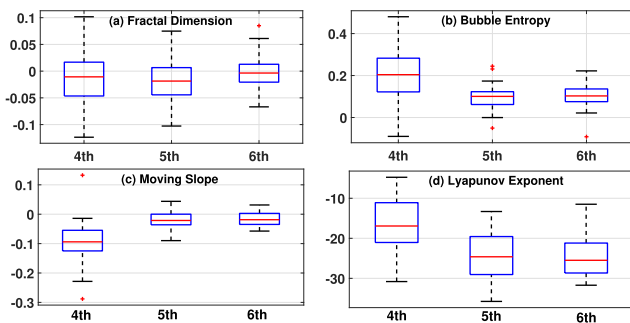


**Fig. 12.** Box plot to illustrate the discrimination behavior of the proposed nonlinear feature values between normal and hypertensive PPG contours in their fourth, fifth, and sixth derivatives. (a) Fractal dimension. (b) BE. (c) Moving slope. (d) Lyapunov exponent.

TABLE V  
ESTIMATION COMPARISON WITH STANDARDS OF BHS

| Cumulative Error frequency | <5mmHg | <10mmHg | <15mmHg |
|----------------------------|--------|---------|---------|
| Grade A                    | 60%    | 85%     | 95%     |
| Grade B                    | 50%    | 75%     | 90%     |
| Grade C                    | 40%    | 65%     | 85%     |
| <b>Systolic BP</b>         | 72.8%  | 92.8%   | 96.8%   |
| <b>Diastolic BP</b>        | 92.6%  | 98.9%   | 99.6%   |

### C. Trade-off in Using Higher PPG Derivatives

The proposed nonlinear features are extracted from the third and fourth derivatives of the PPG cycle. After experimental investigation, we observed that the discrimination potential of these features beyond the fourth derivative decreases as higher derivatives tend to yield symmetrical waveform patterns. Moreover, the frequency range of PPG signal is limited to approximately 5 Hz. We experimented with and analyzed the nonlinear features from the PPG cycles up to the sixth derivative and obtained the discrimination of each feature values computed for the normotensive and hypertensive contours of 100 segments. The box plot of the obtained difference is illustrated in Fig. 12. It is visible that the interquartile range of different errors in the fourth derivative is more extensive than in the fifth and sixth derivatives indicating the broader distribution of errors and hence a good discrimination potential compared with the fifth and sixth derivatives. So, it can be concluded that the proposed features derived up to the fourth derivative are more informative with better discriminating characteristics and valuable for better BP estimation.

### D. Comparison With BHS Standard

The British Hypertension Society (BHS) protocol has allocated a grading system referring to the ambulatory system to appraise the performance of BP measuring devices [45]. The grading criteria are based on the cumulative error thresholds, which require either grade *A* or grade *B* for the recommendation of a BP estimation device by BIH for suitability for consumers. Table V shows each grade's cumulative error frequency range. Our best obtained results on this comparison achieve grade – *A* for SBP and DBP to highlight that the proposed framework is suitable for personalized BP devices with clinical standards.

### V. CONCLUSION

Unlike other physiological signals such as ECG and EEG, it is always challenging to predict the type of pathological event from PPG signals since no significant variations can be observed in their morphology apart from volumetric blood changes. In this study, the nonlinear features of PPG signals have been evaluated using the third and fourth derivatives. Furthermore, these nonlinear features of PPG signals and machine learning models have been used for the estimation of SBP and DBP, respectively. The proposed approach does not require detecting the fiducial points of the PPG signals to evaluate the nonlinear features, and these features are found as discriminative for BP estimation. The results reflect the contribution of these nonlinear attributes in enhancing accuracy in the classification and estimation of cuff-less BP compared with the previously reported similar works. The proposed integrated model carries two separate tasks: estimation and classification to numerically produce the estimated BP values and a label display of the BP class for personalized dynamic BP monitoring. In the estimation domain, it has been observed that the SBP estimation error is higher than DBP because the SBP values are more diverse in all the datasets used when derived from the reference ABP signal. After investigating the MIMIC-II database, the histogram of BP values captured from the reference ABP signal gives a more diverse range of SBP values, ranging from 85 to 230 mmHg compared with DBP 40 to 110 mmHg. Thus, it is harder for the proposed framework to model the variance of SBP, which causes higher estimation errors than in DBP. The proposed model achieved “Grade A” on the BHS standard, which substantiates this work’s robustness for personalized healthcare devices for noninvasive and continuous monitoring of BP.

### REFERENCES

- [1] J. Allen, “Photoplethysmography and its application in clinical physiological measurement,” *Physiol. Meas.*, vol. 28, no. 3, pp. R1–R39, Mar. 2007, doi: 10.1088/0967-3334/28/3/R01.
- [2] S. Park and S. Jayaraman, “Enhancing the quality of life through wearable technology,” *IEEE Eng. Med. Biol. Mag.*, vol. 22, no. 3, pp. 41–48, May 2003.
- [3] F. H. Messerli and B. W. E. Ritz, “Essential hypertension,” *Lancet*, vol. 370, no. 9587, pp. 591–603, 2007.
- [4] S. Gupta, A. Singh, A. Sharma, and R. K. Tripathy, “DSVRI: A PPG-based novel feature for early diagnosis of type-II diabetes mellitus,” *IEEE Sensors Lett.*, vol. 6, no. 9, pp. 1–4, Sep. 2022.
- [5] M. Kachuee, M. M. Kiani, H. Mohammadzade, and M. Shabany, “Cuffless blood pressure estimation algorithms for continuous health-care monitoring,” *IEEE Trans. Biomed. Eng.*, vol. 64, no. 4, pp. 859–869, Apr. 2017.
- [6] Y.-H. Li, L. N. Harfiya, K. Purwandari, and Y.-D. Lin, “Real-time cuffless continuous blood pressure estimation using deep learning model,” *Sensors*, vol. 20, no. 19, p. 5606, Sep. 2020.
- [7] M. S. Tanveer and M. K. Hasan, “Cuffless blood pressure estimation from electrocardiogram and photoplethysmogram using waveform based ANN-LSTM network,” *Biomed. Signal Process. Control*, vol. 51, pp. 382–392, May 2019.
- [8] M. Liu, L. M. Po, and H. Fu, “Cuffless blood pressure estimation based on photoplethysmography signal and its second derivative,” *Int. J. Comput. Theory Eng.*, vol. 9, no. 3, p. 202, 2017.
- [9] N. Hasanzadeh, M. M. Ahmadi, and H. Mohammadzade, “Blood pressure estimation using photoplethysmogram signal and its morphological features,” *IEEE Sensors J.*, vol. 20, no. 8, pp. 4300–4310, Apr. 2020.
- [10] C. El-Hajj and P. Kyriacou, “Deep learning models for cuffless blood pressure monitoring from PPG signals using attention mechanism,” *Biomed. Signal Process. Control*, vol. 65, Mar. 2021, Art. no. 102301.

- [11] C. El-Hajj and P. A. Kyriacou, "Cuffless blood pressure estimation from PPG signals and its derivatives using deep learning models," *Biomed. Signal Process. Control*, vol. 70, Sep. 2021, Art. no. 102984.
- [12] S. Gupta, A. Singh, and A. Sharma, "Dynamic large artery stiffness index for cuffless blood pressure estimation," *IEEE Sensors Lett.*, vol. 6, no. 3, pp. 1–4, Mar. 2022, doi: [10.1109/LSENS.2022.3157060](https://doi.org/10.1109/LSENS.2022.3157060).
- [13] W. Wang, P. Mohseni, K. L. Kilgore, and L. Najafizadeh, "Cuff-less blood pressure estimation from photoplethysmography via visibility graph and transfer learning," *IEEE J. Biomed. Health Informat.*, vol. 26, no. 5, pp. 2075–2085, May 2022.
- [14] O. Schlesinger, N. Vigderhouse, D. Eytan, and Y. Moshe, "Blood pressure estimation from PPG signals using convolutional neural networks and Siamese network," in *Proc. IEEE Int. Conf. Acoust., Speech Signal Process. (ICASSP)*, May 2020, pp. 1135–1139, doi: [10.1109/ICASSP40776.2020.9053446](https://doi.org/10.1109/ICASSP40776.2020.9053446).
- [15] S. S. Chowdhury, R. Hyder, M. S. B. Hafiz, and M. A. Haque, "Real-time robust heart rate estimation from wrist-type PPG signals using multiple reference adaptive noise cancellation," *IEEE J. Biomed. Health Informat.*, vol. 22, no. 2, pp. 450–459, Mar. 2018, doi: [10.1109/JBHI.2016.2632201](https://doi.org/10.1109/JBHI.2016.2632201).
- [16] S. S. Mousavi, M. Firouzmand, M. Charmi, M. Hemmati, M. Moghadam, and Y. Ghorbani, "Blood pressure estimation from appropriate and inappropriate PPG signals using a whole-based method," *Biomed. Signal Process Control*, vol. 47, pp. 196–206, Jan. 2019.
- [17] T. O'Haver, "A pragmatic introduction to signal processing," Univ. Maryland College Park, College Park, MD, USA, Tech. Rep., May 2020.
- [18] A. L. Goldberger et al., "PhysioBank, PhysioToolkit, and PhysioNet: Components of a new research resource for complex physiologic signals," *Circulation*, vol. 101, no. 23, pp. e215–e220, Jun. 2000.
- [19] M. Kachuee, M. M. Kiani, H. Mohammadzade, and M. Shabany, "Cuffless high-accuracy calibration-free blood pressure estimation using pulse transit time," in *Proc. IEEE Int. Symp. Circuits Syst. (ISCAS)*, May 2015, pp. 1006–1009.
- [20] A. E. W. Johnson et al., "MIMIC-III, a freely accessible critical care database," *Sci. Data*, vol. 3, no. 1, pp. 1–9, Dec. 2016.
- [21] I. W. Selesnick. (2011). *TQWT Toolbox Guide*. Electrical and Computer Engineering, Polytechnic Institute of New York University. [Online]. Available: <http://eeweb.poly.edu/iselesni/TQWT/index.html>
- [22] M. Elgendi, Y. Liang, and R. Ward, "Toward generating more diagnostic features from photoplethysmogram waveforms," *Diseases*, vol. 6, no. 1, p. 20, Mar. 2018.
- [23] F. Scholkmann, J. Boss, and M. Wolf, "An efficient algorithm for automatic peak detection in noisy periodic and quasi-periodic signals," *Algorithms*, vol. 5, no. 4, pp. 588–603, 2012.
- [24] P. J. Chowienczyk et al., "Photoplethysmographic assessment of pulse wave reflection: Blunted endothelium-dependent response to beta adrenergic vasodilation in type II diabetes," *J. Amer. College Cardiol.*, vol. 34, pp. 2007–2014, Dec. 1999.
- [25] S. R. Alty, N. Angarita-Jaimes, S. C. Millasseau, and P. J. Chowienczyk, "Predicting arterial stiffness from the digital volume pulse waveform," *IEEE Trans. Biomed. Eng.*, vol. 54, no. 12, pp. 2268–2275, Nov. 2007.
- [26] S. Gupta, A. Singh, and A. Sharma, "Photoplethysmogram based mean arterial pressure estimation using LSTM," in *Proc. 8th Int. Conf. Signal Process. Integr. Netw. (SPIN)*, Aug. 2021, pp. 806–811, doi: [10.1109/SPIN52536.2021.9566027](https://doi.org/10.1109/SPIN52536.2021.9566027).
- [27] S. C. Millasseau, R. P. Kelly, J. M. Ritter, and P. J. Chowienczyk, "Determination of age-related increases in large artery stiffness by digital pulse contour analysis," *Clin. Sci.*, vol. 103, no. 4, pp. 371–377, Oct. 2002.
- [28] E. C.-P. Chua, S. J. Redmond, G. McDarby, and C. Heneghan, "Towards using photo-plethysmogram amplitude to measure blood pressure during sleep," *Ann. Biomed. Eng.*, vol. 38, no. 3, pp. 945–954, Mar. 2010.
- [29] J. Padilla, E. Berjano, J. Saiz, L. Facila, P. Diaz, and S. Merce, "Assessment of relationships between blood pressure, pulse wave velocity and digital volume pulse," in *Proc. Comput. Cardiol.*, Sep. 2006, pp. 893–896.
- [30] M. Elgendi, I. Norton, M. Brearley, D. Abbott, and D. Schuurmans, "Detection of a and b waves in the acceleration photoplethysmogram," *Biomed. Eng. OnLine*, vol. 13, no. 1, p. 139, 2014, doi: [10.1186/1475-925X-13-139](https://doi.org/10.1186/1475-925X-13-139).
- [31] I. Imanaga, H. Hara, S. Koyanagi, and K. Tanaka, "Correlation between wave components of the second derivative of plethysmogram and arterial distensibility," *Jpn. Heart J.*, vol. 39, no. 6, pp. 775–784, 1998.
- [32] S. Kesić and S. Z. Spasić, "Application of Higuchi's fractal dimension from basic to clinical neurophysiology: A review," *Comput. Methods Programs Biomed.*, vol. 133, pp. 55–70, Sep. 2016.
- [33] G. Manis, M. Aktaruzzaman, and R. Sassi, "Bubble entropy: An entropy almost free of parameters," *IEEE Trans. Biomed. Eng.*, vol. 64, no. 11, pp. 2711–2718, Nov. 2017, doi: [10.1109/TBME.2017.2664105](https://doi.org/10.1109/TBME.2017.2664105).
- [34] M. T. Rosenstein, J. J. Collins, and C. J. De Luca, "A practical method for calculating largest Lyapunov exponents from small data sets," *Phys. D, Nonlinear Phenomena*, vol. 65, pp. 117–134, May 1993.
- [35] M. Elgendi, I. Norton, M. Brearley, D. Abbott, and D. Schuurmans, "Detection of A and B waves in the acceleration photoplethysmogram," *Biomed. Eng. OnLine*, vol. 13, no. 1, pp. 1–18, 2014.
- [36] J. D'Errico. (2022). *Movingslope*. [Online]. Available: <https://www.mathworks.com/matlabcentral/fileexchange/16997-movingslope>
- [37] J. K. Jaiswal and R. Samikannu, "Application of random forest algorithm on feature subset selection and classification and regression," in *Proc. World Congr. Comput. Commun. Technol. (WCCCT)*, Feb. 2017, pp. 65–68.
- [38] O. Sagi and L. Rokach, "Approximating XGBoost with an interpretable decision tree," *Inf. Sci.*, vol. 572, pp. 522–542, Sep. 2021.
- [39] Y.-J. Lee, W.-F. Hsieh, and C.-M. Huang, "SSVR: A smooth support vector machine for-insensitive regression," *IEEE Trans. Knowl. Data Eng.*, vol. 17, no. 5, pp. 678–685, May 2005.
- [40] A. V. Chobanian et al., "Seventh report of the joint national committee on prevention, detection, evaluation, and treatment of high blood pressure," *Hypertension*, vol. 42, no. 6, pp. 1206–1252, Dec. 2003.
- [41] D. Chicco, M. J. Warrens, and G. Jurman, "The coefficient of determination R-squared is more informative than SMAPE, MAE, MAPE, MSE and RMSE in regression analysis evaluation," *PeerJ Comput. Sci.*, vol. 7, p. e623, Jul. 2021.
- [42] S. Sharma, M. F. Hashmi, and P. T. Bhattacharya, "Hypotension," in *StatPearls*. Treasure Island, FL, USA: StatPearls, Jan. 2022. Accessed: Feb. 16, 2022. [Online]. Available: <https://www.ncbi.nlm.nih.gov/books/NBK499961/>
- [43] *Multiclass Classification Using Keras*. Accessed: Mar. 8, 2022. [Online]. Available: <https://towardsdatascience.com/multiclass-classification-and-information-bottleneck-an-example-using-keras-5591b9a2c000>
- [44] L. Breiman, "Random forests," *Mach. Learn.*, vol. 1, no. 45, pp. 5–32, 2001.
- [45] E. O'Brien et al., "The British hypertension society protocol for the evaluation of automated and semi-automated blood pressure measuring devices with special reference to ambulatory systems," *J. Hypertension*, vol. 8, no. 7, pp. 607–619, Jul. 1990.